Computational study of the interaction of freely moving particles at intermediate Reynolds numbers

Açmae El Yacoubi[1], Sheng Xu[2] and Z. Jane Wang[1,3]†

[1] Department of Mechanical & Aerospace Engineering, Cornell University, Ithaca, NY 14853, USA

[2] Department of Mathematics, Southern Methodist University, Dallas, TX 75275-0156, USA

[3] Department of Physics, Cornell University, Ithaca, NY 14853, USA

Motivated by our interest in understanding collective behaviour and self-organization resulting from hydrodynamic interactions, we investigate the two-dimensional dynamics of horizontal arrays of settling cylinders at intermediate Reynolds numbers. To simulate these dynamics, we develop a direct numerical simulation based on the immersed interface method. A novel aspect of our method is its ability to efficiently and accurately couple the dynamics of the freely moving objects with the fluid. We report the falling configuration and the wake pattern of the array, and investigate their dependence on the number of particles, n, as well as the initial inter-particle spacing, d_0. We find that, in the case of odd-numbered arrays, the middle cylinder is always leading, whereas in the case of even-numbered arrays, the steady-state shape is concave-down. In large arrays $n \geqslant 5$, the outer pairs tend to cluster. In addition, we analyse detailed kinematics, wakes and forces of three settling cylinders. We find that the middle one experiences a higher drag force in the presence of neighbouring cylinders, compared to an isolated settling cylinder, resulting in a decrease in its settling velocity. For a small initial spacing d_0, the middle cylinder experiences a strong sideway repulsive force, the magnitude of which increases with decreasing d_0. During the fall, the left and right cylinders rotate outwards and shed vortices in anti-phase.

Key words: computational methods, particle/fluid flow

1. Introduction

Collective behaviour and self-organization of particles subject to hydrodynamic interactions are common among a wide range of biological systems and organisms, such as swarming, schooling or flocking (Niwa 1994; Couzin & Krause 2003). Hydrodynamic interactions play an important role in micro-organism colony growth through clustering mechanisms (Pedley & Kessler 1992; Czirók & Vicsek 2006; Cisneros *et al.* 2007; Darnton *et al.* 2010; Gregor *et al.* 2010) and in diffusive mixing (Kim & Breuer 2004; Hernandez-Ortiz, Stoltz & Graham 2005; Saintillan & Shelley 2008; Katija & Dabiri 2009; Thiffeault & Childress 2010). Collective dynamics of

† Email address for correspondence: zw24@cornell.edu

particles is also central to physical phenomena such as cloud formation, particle suspension and particle sedimentation (Warhaft 2009; Guazzelli & Hinch 2011).

At low Reynolds numbers, where the flow is governed by Stokes equations, there have been extensive theoretical, numerical and experimental studies of hydrodynamic interactions of large collections of particles (Hocking 1963; Jayaweera & Mason 1963, 1965; Crowley 1971; Ekiel-Jeżewska, Metzger & Guazzelli 2006; Koch & Subramanian 2011). The linearity of Stokes equations permits the use of the superposition of fundamental solutions (Stokeslets) (Happel & Brenner 1973). For instance, recent work has shown that a spherical cloud of particles settling in a viscous fluid spreads, and eventually evolves into a toroidal shape and separates into a cascade of smaller clumps (Ekiel-Jeżewska *et al.* 2006).

In contrast, at intermediate Reynolds numbers, the dynamics of the particles are further complicated by the fluid inertia, which introduces unsteadiness to these problems. There have been relatively few studies on particle interactions and clustering (Jenny, Dušek & Bouchet 2004; Ardekani & Rangel 2006; Daniel *et al.* 2009) and there appears to be a need to explore the rich dynamics of collections of particles in this regime.

In the present work, we carry out a numerical investigation of multiple interacting particles in the intermediate-Reynolds-number range. The goal of this paper is twofold. First, we introduce a new numerical method for solving the two-dimensional Navier–Stokes equation in the presence of freely moving particles of arbitrary shapes and arbitrary density. The method is a further development of our previous immersed interface method (Xu & Wang 2006*a*, 2007; Xu 2008) and allows simultaneous solution of the dynamics of the particles and the fluid. The method for coupling the fluid and solid dynamics does not introduce additional constraints on the integration time step, hence allowing an efficient simulation of multiple, arbitrarily moving particles. The second goal is to discover a rich set of new dynamics of multiple particles, interacting in a fluid, in the intermediate-Reynolds-number range. In particular, we will focus on the dynamics of arrays of falling cylinders, starting from different initial conditions.

2. Method

To simulate the dynamics of cylinders settling under gravity, we further develop the immersed interface method to simulate the interaction of a fluid with free moving particles. In our previous work (Xu & Wang 2006*a*; Xu 2008), the rigid objects followed a prescribed motion. Here, the dynamics of the freely moving rigid objects are coupled with the surrounding fluid. Below, we introduce an iterative scheme in the immersed interface method to handle this coupling without reducing the accuracy and stability of the method.

2.1. *Equations of motion*

The equations of motion for the fluid are governed by the Navier–Stokes equations subject to boundary conditions on the surfaces of the objects. The dynamics of the immersed objects are governed by Newton's equations. The motions of the fluid and the objects are coupled through the boundary conditions at the objects. In the formulation of the immersed interface method, the fluid velocity $\boldsymbol{v}$ and pressure p outside an object (multiple objects are considered similarly) satisfy:

$$\frac{\partial \boldsymbol{v}}{\partial t} + \boldsymbol{v} \cdot \nabla \boldsymbol{v} = -\nabla p + \frac{1}{Re} \nabla^2 \boldsymbol{v} + \int_{\Gamma} \boldsymbol{f}(\alpha, t)\, \delta(\boldsymbol{x} - \boldsymbol{X}(\alpha, t))\, \mathrm{d}\alpha, \qquad (2.1a)$$
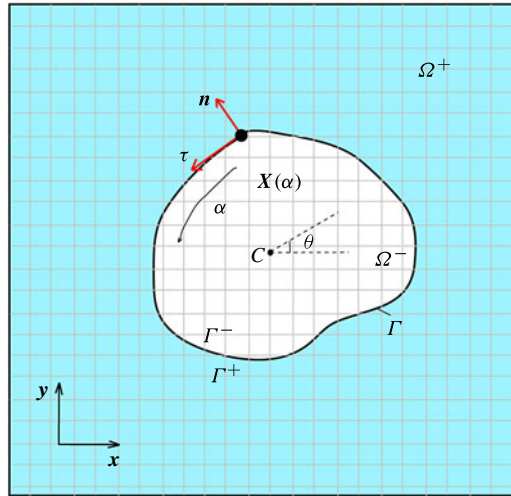
FIGURE 1. (Colour online) Computational domain of an object immersed in a fluid.

$$\nabla \cdot \boldsymbol{v} = 0, \tag{2.1b}$$

where $\boldsymbol{f}$ is the density of a singular force which enforces the boundary condition on the boundary Γ of the object, the boundary Γ is parameterized by α as shown in figure 1, $\delta(\cdot)$ is the two-dimensional Dirac delta function, $\boldsymbol{x}$ is the Cartesian coordinates of the Eulerian fluid, and $\boldsymbol{X}(\alpha, t)$ is the Cartesian coordinates of Lagrangian points on the boundary.

The rigid object is modelled as a rigid fluid. Thus, the velocity of a fluid particle inside is $\boldsymbol{v} = \boldsymbol{v}_c + \boldsymbol{\Omega} \times \boldsymbol{r}$, where $\boldsymbol{\Omega}$ is the angular rotation of the object (in two dimensions, $\|\boldsymbol{\Omega}\|_2 = \dot{\theta}$) and $\boldsymbol{r} = \boldsymbol{x} - \boldsymbol{x}_c$ is the position of the fluid particle relative to the centre of mass $\boldsymbol{x}_c$ of the object. Hence, the acceleration of the fluid particle is

$$\frac{\mathrm{d}\boldsymbol{v}}{\mathrm{d}t} = \underbrace{\frac{\mathrm{d}\boldsymbol{v}_c}{\mathrm{d}t} + \boldsymbol{\Omega} \times (\boldsymbol{\Omega} \times \boldsymbol{r})}_{-\nabla p} + \underbrace{\frac{\mathrm{d}\boldsymbol{\Omega}}{\mathrm{d}t} \times \boldsymbol{r}}_{f_b}. \tag{2.2}$$

The first two terms can be expressed as gradient of pressure and the last term is an additional body force $\boldsymbol{f}_b$ associated with the angular acceleration of the object. Inside the object, $\nabla^2 \boldsymbol{v} = \boldsymbol{0}$, and the pressure is

$$p = -\frac{\mathrm{d}^2 x_c}{\mathrm{d}t^2} x - \frac{\mathrm{d}^2 y_c}{\mathrm{d}t^2} y + \frac{1}{2} \Omega^2 ((x - x_c)^2 - (y - y_c)^2). \tag{2.3}$$

Finally, the equations of motion for the object are

$$m_s \dot{\boldsymbol{v}}_c = \boldsymbol{F}_{ext} + \boldsymbol{F}_f, \tag{2.4a}$$

$$I^* \ddot{\theta} = T_f, \tag{2.4b}$$

where m_s is its mass, I^* its moment of inertia with respect to its centre of mass, $\boldsymbol{F}_{ext}$ is the external non-fluid force on the object, $\boldsymbol{F}_f$ is the fluid force on the object, and T_f is the fluid torque on the object with respect to its centre of mass.

Equations (2.1)–(2.4) constitute the coupled equations for the fluid and the solid that we will solve.

The singular force distribution in (2.1*a*) is related to the jumps in the fluid variables and their derivatives across the fluid–object interface (Xu & Wang 2006*a*,*b*; Xu 2008). The tangential and normal components of the singular force in (2.1*a*) are given by

$$f_\tau = \boldsymbol{f} \cdot \boldsymbol{\tau} = -\frac{1}{Re}\left(\boldsymbol{\tau} \cdot \left.\frac{\partial \boldsymbol{v}}{\partial n}\right|_{\Gamma+} - \frac{\mathrm{d}\theta}{\mathrm{d}t}\right), \tag{2.5a}$$

$$f_n = \boldsymbol{f} \cdot \boldsymbol{n} = \int \left(\frac{1}{Re}\left.\frac{\partial \omega}{\partial n}\right|_{\Gamma+} + [\boldsymbol{f}_b] \cdot \boldsymbol{\tau}\right) J \,\mathrm{d}\alpha, \tag{2.5b}$$

where $\omega = (\partial v/\partial x) - (\partial u/\partial y)$ is the vorticity, $\boldsymbol{\tau} = (\partial \boldsymbol{X}/J\partial\alpha)$ $(J = \|\partial \boldsymbol{X}/\partial\alpha\|_2)$ and $\boldsymbol{n}$ are the unit tangent and unit normal vectors to the boundary Γ, the brackets $[\cdot] = (\cdot)_{\Gamma+} - (\cdot)_{\Gamma-}$ are used to denote a jump across the interface, and the jump in the tangential component of the body force in (2.5*b*) is

$$[\boldsymbol{f}_b] \cdot \boldsymbol{\tau} = -\frac{\mathrm{d}^2\theta}{\mathrm{d}t^2}((X - x_c)\tau_y - (Y - y_c)\tau_x). \tag{2.6}$$

The fluid force and torque acting on the object can be expressed through the integrals of the singular force

$$\boldsymbol{F}_f = -\int_\Gamma (f_\tau\boldsymbol{\tau} + p^+\boldsymbol{n}) J \,\mathrm{d}\alpha, \tag{2.7a}$$

$$\boldsymbol{T}_f = -\int_\Gamma (\boldsymbol{X} - \boldsymbol{x}_c) \times (f_\tau\boldsymbol{\tau} + p^+\boldsymbol{n}) J \,\mathrm{d}\alpha. \tag{2.7b}$$

2.2. *Dimensionless parameters*

In the computations presented here, we non-dimensionalize the equations by ρ_f, the fluid density, L, a reference length of the object (diameter of the cylinder, width of the plate), V, a reference velocity (terminal velocity of a falling object, associated with a unit-coefficient drag force), and $T = L/V$, the corresponding time scale. The Reynolds number Re is defined as $Re = \rho_f VL/\mu$, where μ is the dynamic fluid viscosity. The non-dimensional mass of the object is $m_s = \gamma\mathscr{A}$, where $\gamma = \rho_s/\rho_f$ is the density ratio between the object and the fluid, and $\mathscr{A}$ is the non-dimensional area of the object. In the cases we will study, $\boldsymbol{F}_{ext} = m\boldsymbol{g}$. The non-dimensional gravity is $\bar{g} = gL/V^2$, where g is the gravitational constant. Because the reference velocity is obtained by equating the buoyancy-corrected weight of the object with a unit-coefficient drag force acting on it, $V = \sqrt{2(\gamma - 1)gL\mathscr{A}}$, $\bar{g}$ depends only on the density ratio and the geometry of the object, $\bar{g} = 1/(2(\gamma - 1)\mathscr{A})$. The gravitational force (the buoyancy-corrected weight) on the object is $\boldsymbol{F}_g = (\gamma - 1)\mathscr{A}\bar{g}$. In summary, there is a total of five non-dimensional parameters, $Re, \bar{g}, \gamma, n, d_0$, where n is the number of objects and d_0 is the initial spacing between them. In this paper, we focus on the effect of n and d_0 on the dynamics.

2.3. *Numerical implementation*

In the immersed interface method, (2.1) are solved on a fixed grid by incorporating into a numerical scheme jump conditions across fluid–object interfaces (Xu & Wang 2006*b*). The jump conditions are induced by and related to singular forces. A main difficulty in the numerical treatment of a freely moving object, compared to an object under prescribed motion (Xu & Wang 2006*a*; Xu 2008), is the coupling of the dynamics of the fluid with the object. The pressure external to the object depends explicitly on the normal component of the singular force, and thus on the angular

acceleration of the object, as implied by (2.5*b*) and (2.6). The angular acceleration, in turn, depends on the pressure.

The pair of unknown variables, the pressure p in the fluid and the angular acceleration q of the freely moving objects in the fluid, are governed by two coupled linear systems:

$$Lp + Cq = r, \quad q = Sp + d, \tag{2.8}$$

where p is the pressure defined on a discrete lattice, q is the vector formed by the angular acceleration of all the objects, L is a discrete Laplacian, C and S are coupling matrices, and r and d are known vectors. To solve the coupled systems efficiently, we apply an augmented variable approach (Li *et al.* 2006) using the generalized minimal residual method (GMRES). By eliminating p from (2.8), we obtain the Schur-complement system for q:

$$(E + SL^{-1}C)q = d + SL^{-1}r \tag{2.9}$$

where E is the identity matrix. q can be solved for iteratively using GMRES, and consequently, p can be determined from (2.8).

We note that the GMRES iteration does not require the explicit form of L, C, S and $E + SL^{-1}C$. Instead, it only needs the matrix–vector product $(E + SL^{-1}C)q^{(k)}$, where $q^{(k)}$ is a guess solution at the kth step. In the kth step, we use the guess solution $q^{(k)}$ to solve for $p^{(k)}$, and use $p^{(k)}$ to compute $q^{(k+1)}$. It can be shown that the right-hand-side vector $d + SL^{-1}r$ in the Schur-complement system is Q_0, where Q_0 is the value of q after the first iteration with zero initial guess. The matrix–vector product $(E + SL^{-1}C)q^{(k)}$ in the kth step is

$$(E + SL^{-1}C)q^{(k)} = Q_0 - q^{(k+1)} + q^{(k)}. \tag{2.10}$$

The GMRES iteration converges when $q^{(k+1)} = q^{(k)}$.

With the exception of the handling of the coupling between the fluid and the objects, the remainder of the numerical implementation in the present study is similar to that in Xu & Wang (2006*a*) and Xu (2008). The momentum equations, (2.1*a*), are solved using finite differences on a MAC grid. The time integration is an explicit fourth-order Runge–Kutta scheme, and the discrete pressure Poisson equation is solved via fast Fourier transform.

We carried out a grid-resolution analysis to test the convergence of our current implementation. The results show that it is second-order accurate, including along the boundaries of the objects. In addition, we observe that GMRES used in solving the Schur-complement system converges in only a few iterations, even for a large number of freely moving objects.

3. Code validation

The novel aspect of our current implementation of the immersed interface method is the ability to handle freely moving objects in a fluid. To validate the new features of our code, we compare our results with experiments on freely fluttering and tumbling plates.

Andersen, Pesavento & Wang (2005*a*,*b*) and Pesavento & Wang (2004) experimentally and numerically investigated the dynamics of falling rectangular plates. Their study provides qualitative and quantitative data on different falling modes, including fluttering, tumbling and chaotic motion, which we use to test the current code.
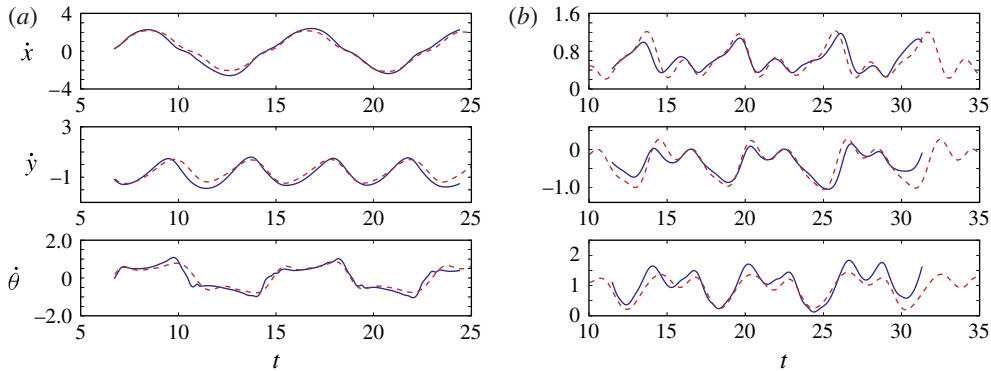
FIGURE 2. (Colour online) Comparison between experiments in Andersen *et al.* (2005*a*) (dashed, red online) and the current simulations (solid, blue online) on (*a*) a fluttering plate with $I^* = 0.16$, $Re = 1147$ and $\beta = 1/14$ and (*b*) a tumbling plate with $I^* = 0.48$, $Re = 737$ and $\beta = 1/5$. From top to bottom: *x*-velocity, *y*-velocity and angular velocity $\dot{\theta}$ of the plate.

Parameters	Fluttering	Tumbling
(β, I^*, Re)	(1/14, 0.16, 1147)	(1/5, 0.48, 737)
θ_0	20°	45°
$(\dot{x}_c, \dot{y}_c, \dot{\theta})_{t=0}$	(0, 0, 0.5)	(0, 0, 0.5)

TABLE 1. Simulation parameters for the fluttering and tumbling motion of a rounded-rectangular plate, using the immersed interface method.

In our simulations, we use rounded-rectangular plates, similar to the experimental geometry, as opposed to ellipses (Pesavento & Wang 2004). The rounded plate has a smaller curvature at the tips and can be resolved numerically with fewer grid points. Given the difference in the plate geometries, and in order to match both the thickness-to-width ratio β and the non-dimensional moment of inertia $I^* = I/\rho_f L^4$, the density of the plates in the current study is slightly different from that in the experiments. The length scale is the width of the plate, the velocity scale is defined as the terminal velocity of the plate falling with unit drag coefficient, $V = \sqrt{2(\gamma - 1)gL\mathscr{A}}$, and the time scale is $T = L/V$. We reproduce the fluttering and tumbling cases in Andersen *et al.* (2005*a*) and summarize our comparisons on figure 2 and table 2. In these computations, the grid resolution is 1600×3200, for domain size 10×20, and the time step is $\Delta t = 5 \times 10^{-3}$, with the initial conditions specified in table 1. In both cases, at steady state, the results match very well and the small difference may be attributed to the plate geometry.

4. The dynamics of interacting cylinders in two-dimensional flow

In this section, we simulate horizontal arrays of settling cylinders at Reynolds number 200 and investigate the falling pattern and the connection between the dynamics of the particles and of the flow.

At zero Reynolds number, an array of settling spheres can exhibit a rich set of dynamics due to instabilities when the number of particles is sufficiently large

Parameters	Andersen *et al.* (2005*a*)	Current
$(\langle \dot{x}_c \rangle, \langle \dot{y}_c \rangle, \langle \dot{\theta} \rangle)$	$(0.60, -0.34, 0.88)$	$(0.58, -0.37, 0.99)$
Descent slope	$29.2°$	$29.6°$
Period: (short glide, long glide)	$(1.1, 3.2)$	$(1.2, 3.5)$

TABLE 2. Comparison between experimental results in Andersen *et al.* (2005*a*) and the current numerical results for a tumbling plate. $\langle \dot{x}_c \rangle$, $\langle \dot{y}_c \rangle$ and $\langle \dot{\theta} \rangle$ are the average horizontal, vertical and angular velocities, respectively.

(Jayaweera & Mason 1963, 1965; Crowley 1971; Metzger, Nicolas & Guazzelli 2007). For example, Jayaweera & Mason (1963) observed that clusters of less than seven spheres remain in a horizontal plane during the fall, spread out and tend to arrange themselves into regular polygonal shapes. More recently, Metzger *et al.* (2007) found that a spherical cluster of spheres settling under gravity in a viscous flow is unstable and evolves into a torus before breaking up into smaller clusters.

At intermediate Reynolds numbers, the interactions between particles are complicated by the inertial effects. In our case, each cylinder will create a wake that extends for many diameter lengths and leads to non-local and time-dependent interactions. The forces experienced by each cylinder will be unsteady. It is therefore unclear, for a given set of initial conditions, whether the cylinders will approach a steady state, and how the steady-state configuration might depend on the initial arrangement. The steady state of a single particle is attained when the mean velocity, averaged over each period, is constant.

Finally, our current study is restricted to the cases where there is no collision and where the distance between particles can be well-resolved by the immersed interface method. For cases where the initial spacing is sufficiently small, we observe that the particles are likely to collide in close encounter. To resolve the collision dynamics, we are currently developing a method to handle particle collisions.

4.1. *Falling pattern at steady state*

In what follows, we study the dynamics of a horizontal array of *n* falling cylinders. We present a qualitative comparison of the falling patterns of the array. First, we fix the initial spacing, d_0, and vary the number of cylinders $n \in \{3, 4, 5, 6, 7, 8\}$. At a given time, the spacing *d* is defined as the distance between the centres of two adjacent cylinders, hence $d = D + l$ where *D* is the diameter and *l* is the closest distance between their surfaces. The grid size and the time step are fixed at $\Delta x = \Delta y = 1/40$ and $\Delta t = 5 \times 10^{-3}$, respectively. The domain varies between 40×96 and 48×72, depending on the number of objects. We choose no-slip boundary conditions on all four fixed walls of the domain. This avoids specifying the far-field boundary conditions on a finite computational domain, in an unbounded fluid, which would involve modelling the wake of the objects.

Figure 3(*a*) shows trajectories of the settling cylinders. When *n* is odd, the middle cylinder is always leading. Conversely, when it is even, the falling shape of the array at steady state is concave-down, provided that the initial spacing is not too small and no collisions occur. Regardless of the value of *n*, at steady state the array displays a left and right mirror symmetry in the vortex shedding pattern and correspondingly, a mirror symmetry in the particle rotation. In other words, two particles symmetric about the centreline rotate in opposite directions and shed counter-rotating vortices
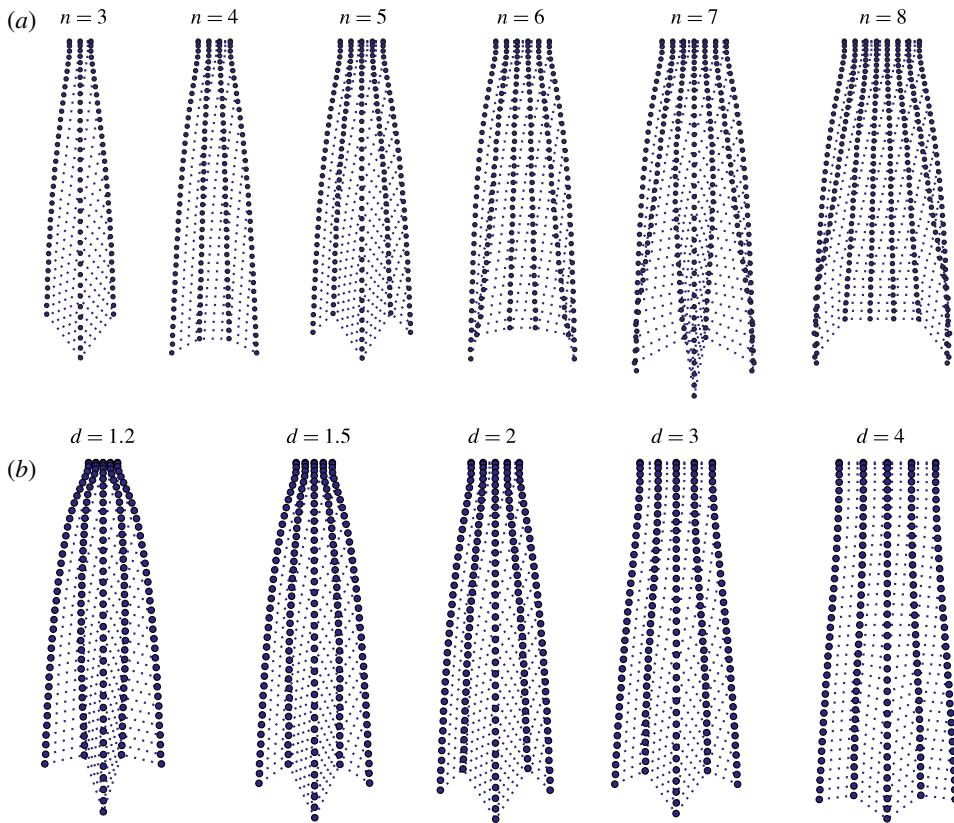
FIGURE 3. (Colour online) Effect on the array falling pattern of (*a*) the number of cylinders, *n*, with $d_0 = 2$ fixed, and (*b*) the initial spacing, d_0, with $n = 5$ fixed. Snapshots are taken every $\delta t = 2$.
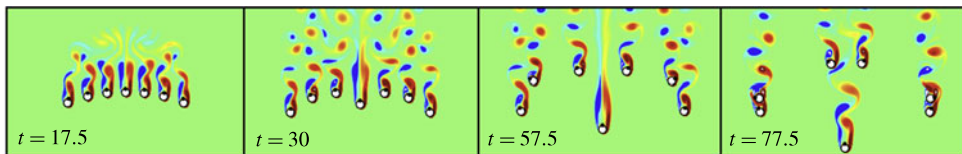
FIGURE 4. (Colour online) Vorticity contours for $n = 7$ falling cylinders with initial spacing $d_0 = 2$. Clustering of the outermost pairs. Black dots on each cylinder are used to visually track their rotation.

(see figure 5 below). This is consistent with the conservation of the total angular momentum, noting that particles are initially dropped with zero angular momentum and the flow field is antisymmetric.

When $n \geqslant 5$, the two outermost cylinders tend to cluster. For example, when $n = 7$ (figures 3*a*, 4), the two leftmost cylinders form a pair and tumble counter-clockwise. Similarly, the rightmost pair tumbles clockwise. The particles do not come into contact and their dynamics are reminiscent of the 'drafting, kissing and tumbling' in fluidized
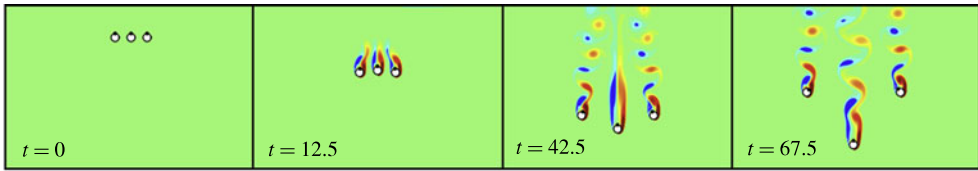
FIGURE 5. (Colour online) Vorticity contours for $n = 3$ falling cylinders with initial spacing $d_0 = 2$. Black dots on each cylinder are used to visually track their rotation.

beds of spheres (Fortes, Joseph & Lundgren 1987). The long-term dynamics of these clusters, $t > 77.5$ on figure 4, will be further investigated in our future work.

We now allow the initial spacing d_0 to vary, while fixing the number of cylinders to $n = 5$. We summarize the effects of d_0 on the falling pattern in figure 3(*b*). We notice that the steady-state configuration depends on the initial spacing. In particular, for the smallest d_0 that was simulated ($d_0 = 1.2$), the immediate neighbours of the middle cylinder approach the centreline, unlike in the other cases. In addition, the spread (or lateral drift) of the array is larger for smaller d_0 owing to the strong interaction force during the early stages of the fall.

Together, these results suggest that arrays of falling cylinders, in an initial horizontal arrangement, can reach a steady state, the final configuration of which depends on d_0 and n. There has been relatively little study on falling cylinders at a similar Reynolds number to compare our results with. One previous study (Singh *et al.* 1989) suggested that an infinite array of cylinders is initially unstable subject to a perturbation to its horizontal configuration. Our results further show that the array will eventually reach a stable configuration. The final configuration deviates significantly from the horizontal.

4.2. *Dynamics of the falling array*

We now provide quantitative data and analyse the dynamics of three settling cylinders. In particular, we quantify the settling velocity, the flow history, the onset of vortex shedding, and the direction and rate of rotation of the cylinders. We will compare these dynamics for different initial spacings, as well as with the dynamics of an isolated settling cylinder. In addition, we will compare our results with those in Stokes flow.

Figure 5 shows the vorticity field of the fall of three cylinders with initial spacing $d_0 = 2$. As they settle, the array spreads out, the middle cylinder leads as it approaches a steady state, the left and right cylinders rotate in opposite directions and their wakes are symmetric about the centreline of the domain. The lateral expansion of the array is due to the strong initial repulsive force, as shown in figure 6(*a*) at $t \approx 7.5$. In this case, the cylinders reach a steady state at $t \sim 100$, as shown in figure 6(*b*).

To gain more insight into the dynamics of the middle cylinder, we first compare it to those of an isolated settling cylinder, under the same flow conditions. Then, we investigate the effect of the initial spacing d_0 on its kinematics and forces. Figure 7 shows the time series of the settling velocity, v, the drag coefficient, C_D, and the lateral force C_x, for the middle cylinder. The effective drag coefficient is larger than for an isolated one, due the presence of co-moving neighbours, and this leads to a decrease in the settling speed. The increase in drag is consistent with the previous computation of two cylinders moving in parallel at similar Reynolds numbers (Wang & Russell 2007). In contrast, in Stokes flow, the presence of neighbouring particles causes a decrease in the drag force. This, in turn, results in an increase in the settling
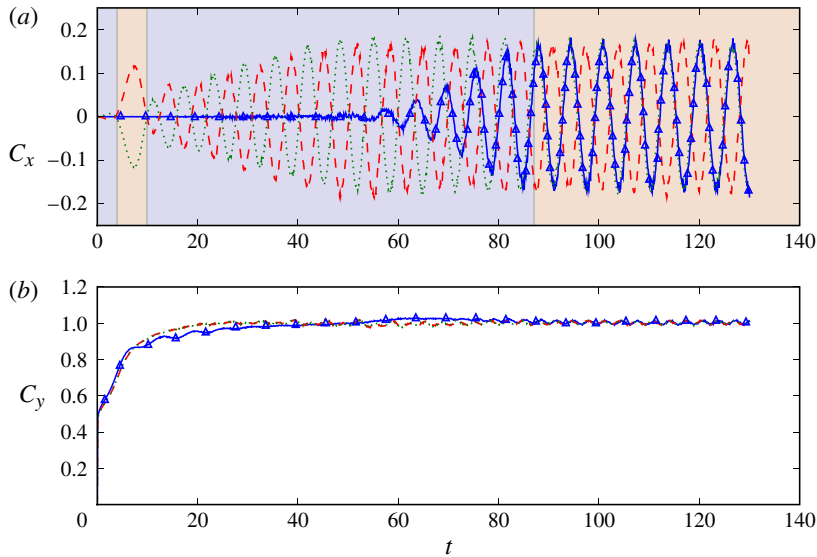
FIGURE 6. (Colour online) Time series of the lateral (C_x) and vertical (C_y) fluid force on three settling cylinders. The blue solid line with triangles is for the middle cylinder, the red dashed line for the right cylinder, and the green dotted line for the left cylinder. The shaded regions in the top figure correspond to the initial weak attraction, followed by a strong repulsion, and a subsequent transition to steady state. The bottom figure shows that the three cylinders attain a dynamic steady state at $t \sim 95$. $Re = 200$ and the initial spacing $d_0 = 2$.

velocity (Happel & Brenner 1973). The drag coefficient C_D for $d_0 = 1.1$ is smaller than for $d_0 = 1.5$ and $d_0 = 2$ initially, but becomes greater than the other two after the onset of shedding. This is consistent with the cross-over in the fluid force. The net force on a particle is shown in figure 8(*h*) ($\ddot{y}$ versus *t*). We can read the fluid force by shifting the curve up by a constant gravitational force. The fluid force for the case $d_0 = 1.1$ shows a cross-over similar to that seen in figure 7, although occurring at a different time because the drag coefficient is drag normalized by $\rho_f U^2(t)L/2$.

At steady state, the drag force does not differ much from the isolated cylinder case, and it differs mainly during the initial and transient stages where it is higher for the other three cases, resulting in a smaller settling velocity.

The settling velocity of an isolated cylinder reaches a maximum at $t \approx 57$. A closer look at figure 7 shows that this corresponds to the onset of vortex shedding. On the other hand, in the presence of its neighbours, the middle cylinder experiences wake instabilities much earlier during the fall, around $t \approx 18$ for small d_0. As a comparison, for flow past a fixed cylinder at $Re = 200$, $t_{vs} \approx 20$, where t_{vs} is the time marking the onset of vortex shedding. The difference in t_{vs} underscores the difference between flow past a fixed cylinder and flow around a cylinder settling at steady state in a quiescent flow, due to the effect of the flow history. Given these results, we quantify the dynamics of the middle cylinder by varying d_0 from 1.1 to 3 and choose to present three representative values $d_0 = 1.1, 1.5, 2$, and summarize the results in figure 8.

As mentioned above, the smaller d_0 is ($d_0 = 1.1$), the faster the middle cylinder settles initially, the sooner its wake symmetry is broken due to early vortex shedding and the sooner it reaches a steady state ($t_{vs} \approx 18, 50, 57$ for $d_0 = 1.1, 1.5, 2$, respectively). At steady state, and independently of the value of d_0, the middle cylinder
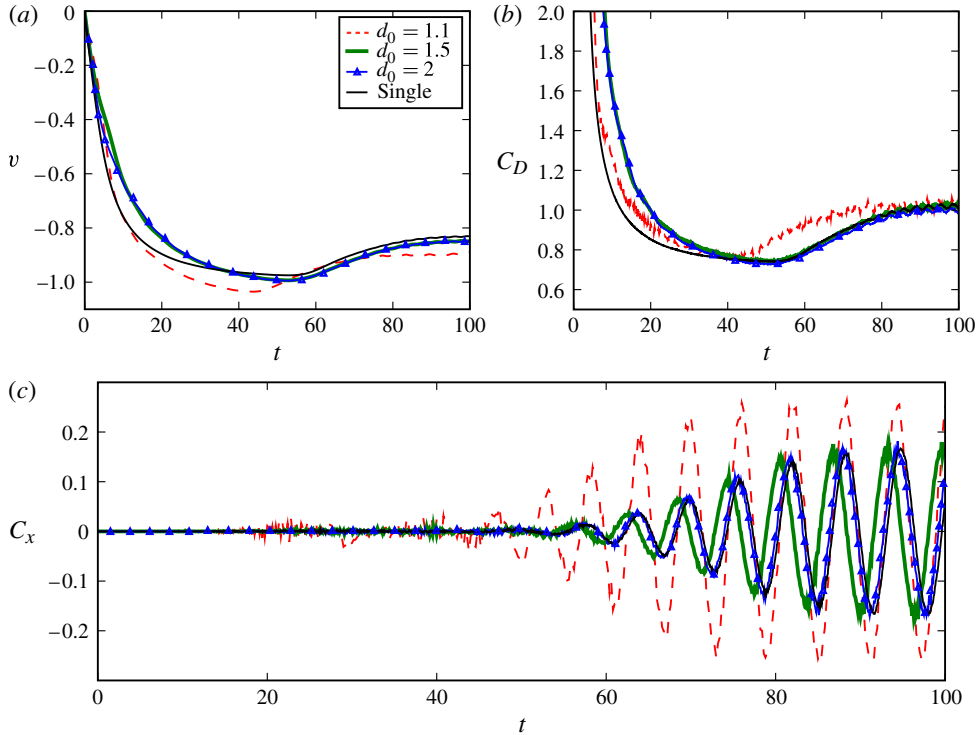
FIGURE 7. (Colour online) Effect of the initial spacing on (*a*) the settling velocity, (*b*) the drag coefficient, and (*c*) the onset of vortex shedding, for the middle cylinder. Comparison with an isolated falling cylinder.

sheds vortices which are in phase with those of either the left or the right cylinder. The non-dimensional shedding frequency in the horizontal direction is the same for all d_0 and is $S_{t,x} = fD/V \approx 0.157$–$0.158$. This can be seen in the time series of the lateral force, C_x, on figure 7(*c*), or the acceleration, $\ddot{x}$, and the velocity, $\dot{x}$, on figure 8(*d,g*).

Similar to fluttering plates or flow-induced vibrations over a fixed cylinder, the oscillation frequency of the middle cylinder along the flow is twice that across it. This can be explained through figure 9. The fluid force vector on the cylinder oscillates between points *A* and *B*. When it goes from *A* to *B*, its *y*-component C_y undergoes a full cycle and comes back to the starting value, but its *x*-component C_x undergoes only a half-cycle and changes sign.

Finally, figure 5 shows that the left and right cylinders rotate outwards, i.e. clockwise for the left one and counter-clockwise for the right one. Correspondingly, their shed vortices have mirror symmetry with respect to the centreline of the domain.

For arbitrary *n*, the outer pair rotates outwards. The inner cylinders, however, rotate inwards as shown on figure 10. When the inter-particle gap is below half a diameter, it is noticeable that the rate of rotation and lateral spread of the side cylinders increase as the inter-particle gap decreases.

5. Conclusions and future work

In this paper, we have studied the falling pattern and dynamics of a horizontal array of settling cylinders at Reynolds number 200, using direct numerical simulation. Given
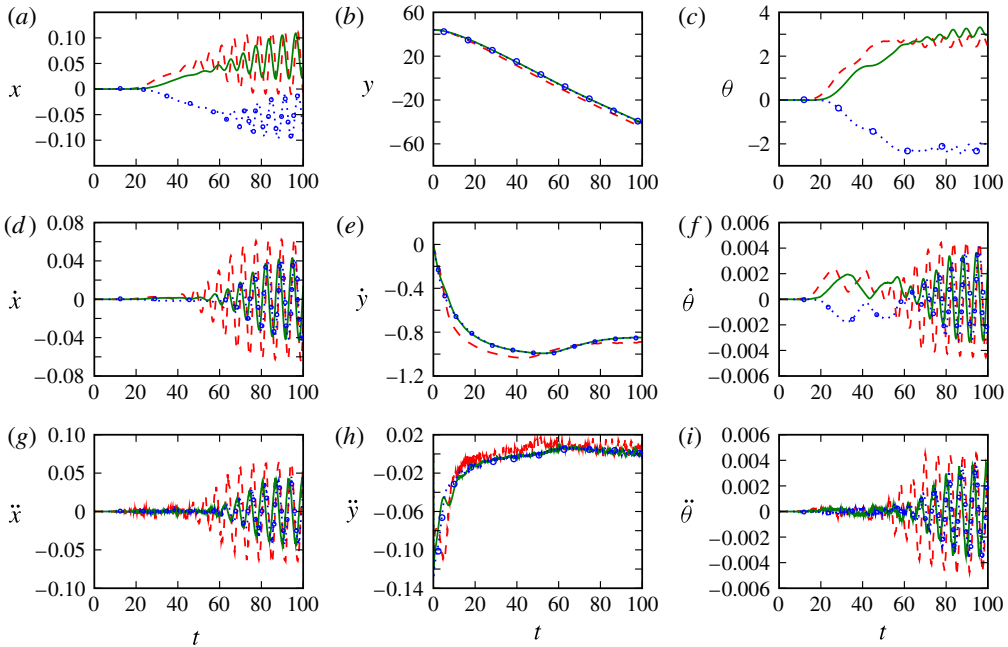
FIGURE 8. (Colour online) Dynamics of the middle cylinder in a 3-cylinder settling array for different values of the initial spacing, d_0. $d_0 = 1.1$ (dashed line, red online), $d_0 = 1.5$ (continuous line, green online) and $d_0 = 2$ (dotted line with circles, blue online). $Re = 200$.
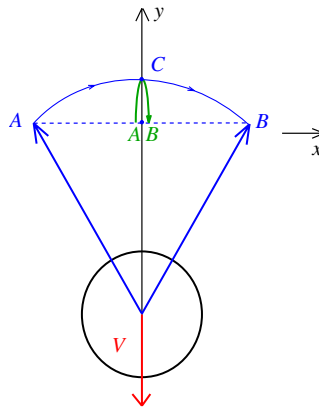
FIGURE 9. (Colour online) Oscillation frequency of the force on the falling cylinder in the streamwise (y) and cross-stream (x) directions. The oscillation frequencies satisfy $f_y = 2f_x$.

the unsteadiness of the flow, we asked whether such a system exhibits a steady state and if so, how it depends on the initial conditions. We investigated the dependence of the falling dynamics on the number of cylinders, n, and on the initial spacing, d_0. We found that the cylinders reach a dynamic steady state independent of the value of n or d_0. The steady configuration depends both on n and d_0. When n is odd, the middle cylinder is always leading, whereas when n is even, the array adopts a
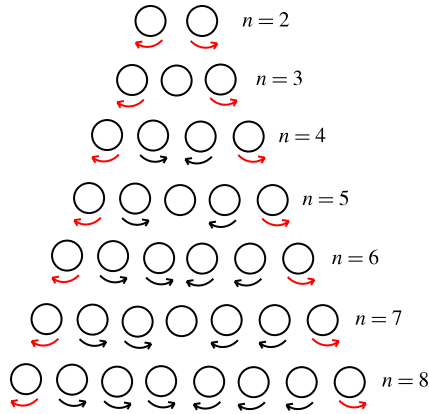
FIGURE 10. (Colour online) Steady-state rotation pattern of the array of cylinders as a function of their number n.

concave-down shape. We then fixed $n = 3$ and studied the effect of the initial spacing on the dynamics of the middle cylinder. We compared them to those of an isolated settling cylinder as well as to results in Stokes flow. We found that the middle cylinder experiences a higher drag force due to the presence of its left and right neighbours, resulting in a slower settling velocity. This result is opposite to that in the Stokes regime where a sphere in the presence of its neighbours settles faster than an isolated one. Our results also showed that the closer the initial spacing is, the sooner wake asymmetries arise for the middle cylinder and the sooner it settles to a steady state. At steady state, for all values of d_0, there is a left–right symmetry in the falling configuration, the wake pattern and the direction of rotation of the left and right cylinders, with respect to the centreline of the domain.

To solve for these dynamics, we developed a robust implementation of the immersed interface method. The novel aspect of this implementation is an efficient handling of the coupling between the rigid body and the fluid, using an iterative method. The method is stable at high Reynolds numbers, at standard CFL (Courant-Friedrichs-Levy) conditions. The method is almost second-order accurate, including along the interface. The code was validated against experiments on falling plates in a fluid. This method provides an efficient tool for us to further investigate collective behaviour and self-organization of particles subject to hydrodynamic interactions.

Acknowledgements

REFERENCES

ANDERSEN, A., PESAVENTO, U. & WANG, Z. J. 2005*a* Unsteady aerodynamics of fluttering and tumbling plates. *J. Fluid Mech.* **541**, 65–90.

ANDERSEN, A., PESAVENTO, U. & WANG, Z. J. 2005*b* Analysis of transitions between fluttering, tumbling and steady descent of falling cards. *J. Fluid Mech.* **541**, 91–104.

ARDEKANI, A. M., DABIRI, S. & RANGEL, R. H. 2008 Collision of multi-particle and general shape objects in a viscous fluid. *J. Comput. Phys.* **227**, 10094–10107.

ARDEKANI, A. M. & RANGEL, R. H. 2006 Unsteady motion of two solid spheres in Stokes flow. *Phys. Fluids* **18**, 103306.

BEARMAN, P. W. & WADOCK, A. J. 1973 The interaction between a pair of circular cylinders normal to a stream. *J. Fluid Mech.* **61**, 499–511.

CISNEROS, L. H., CORTEZ, R., DOMBROWSKI, C., GOLDSTEIN, R. E. & KESSLER, J. O. 2007 Fluid dynamics of self-propelled microorganisms, from individuals to concentrated populations. *Exp. Fluids* **43**, 737–753.

COUZIN, I. D. & KRAUSE, J. 2003 Self-organization and collective behaviour in vertebrates. *J. Adv. Study Behav.* **32**, 1–75.

CROWLEY, J. M. 1971 Viscosity induced instability of a one-dimensional lattice of falling spheres. *J. Fluid Mech.* **45**, 151–159.

CZIRÓK, A. & VICSEK, T. 2006 Collective behaviour of interacting self-propelled particles. *Physica* A **281**, 17–29.

DANIEL, W. B., ECKE, R. E., SUBRAMANIAN, G. & KOCH, D. 2009 Clusters of sedimenting high-Reynolds-number particles. *J. Fluid Mech.* **625**, 371–385.

DARNTON, N. C., TURNER, L., ROJEVSKY, S. & BERG, H. C. 2010 Dynamics of bacterial swarming. *Biophys. J.* **98** (10), 2082–2090.

EKIEL-JEŻEWSKA, M. L., METZGER, B. & GUAZZELLI, É. 2006 Spherical cloud of point particles falling in a viscous fluid. *Phys. Fluids* **18**, 038104.

FORTES, A. F., JOSEPH, D. D. & LUNDGREN, T. S. 1987 Nonlinear mechanics of fluidization of beds of spherical particles. *J. Fluid Mech.* **177**, 467–483.

GREGOR, T., FUJIMOTO, K., MASAKI, N. & SAWAI, S. 2010 The onset of collective behaviour in social amoebae. *Science* **328** (5981), 1021–1025.

GUAZZELLI, É. & HINCH, J. 2011 Fluctuations and instability in sedimentation. *Annu. Rev. Fluid Mech.* **43**, 97–116.

HAPPEL, J. & BRENNER, H. 1973 Low Reynolds number hydrodynamics: with special applications to particulate media. In *Mechanics of Fluids and Transport Processes*. Springer.

HAPPEL, J. & PFEFFER, R. 1960 The motion of two spheres following each other in a viscous fluid. *AIChE J.* **6**, 129.

HERNANDEZ-ORTIZ, J. P., STOLTZ, C. G. & GRAHAM, M. D. 2005 Transport and collective dynamics in suspensions of confined swimming particles. *Phys. Rev. Lett.* **95**, 204501.

HILL, R. J., KOCH, D. L. & LADD, A. J. C. 2001 The first effects of fluid inertia on flows in ordered and random arrays of spheres. *J. Fluid Mech.* **448**, 213–241.

HOCKING, L. M. 1963 The behaviour of clusters of spheres falling in a viscous fluid. Part 2. Slow motion theory. *J. Fluid Mech.* **20**, 129–139.

JAYAWEERA, K. O. L. F. & MASON, B. J. 1963 The behaviour of clusters of spheres falling in a viscous fluid. Part 1. Experiment. *J. Fluid Mech.* **20**, 121–128.

JAYAWEERA, K. O. L. F. & MASON, B. J. 1965 The behaviour of freely falling cylinders and cones in a viscous fluid. *J. Fluid Mech.* **22**, 709–720.

JENNY, M., DUŠEK, J. & BOUCHET, G. 2004 Instabilities and transition of a sphere falling or ascending freely in a Newtonian fluid. *J. Fluid Mech.* **508**, 201–239.

KAISER, D. 2007 Bacterial swarming: a re-examination of cell-movement patterns. *Curr. Biol.* **17**, 561–570.

KANG, S. 2003 Characteristics of flow over two circular cylinders in a side-by-side arrangement at low Reynolds numbers. *Phys. Fluids* **15**, 9.

KATIJA, K. & DABIRI, J. O. 2009 A viscosity-enhanced mechanism for biogenic ocean mixing. *Nature* **460**, 624–626.

KIM, I., ELGHOBASHI, S. & SIRIGNANO, W. 2005 Three-dimensional flow over two spheres placed side by side. *J. Fluid Mech.* **246**, 465.

KIM, M. & BREUER, K. S. 2004 Enhanced diffusion due to motile bacteria. *Phys. Fluids* **16**, L78.

KOCH, D. L. & SUBRAMANIAN, G. 2011 Collective hydrodynamics of swimming microorganisms: living fluids. *Annu. Rev. Fluid Mech.* **43**, 637–659.

LEGENDRE, D., MAGNAUDET, J. & MOUGIN, G. 2003 Hydrodynamic interactions between two spherical bubbles rising side by side in a viscous fluid. *J. Fluid Mech.* **497**, 133–166.

LEICHTBERG, S., WEINBAUM, S., PFEFFER, R. & GLUCKMAN, J. 1976 A study of unsteady forces at low Reynolds number: a strong interaction theory for the coaxial settling of three or more spheres. *Phil. Trans. R. Soc. Lond.* A **282** (1311), 585–610.

LEVEQUE, R. J. & LI, Z. 1994 The immersed interface method for elliptic equations with discontinuous coefficients and singular sources. *SIAM J. Numer. Anal.* **31** (4), 1019–1044.

LI, Z., WAN, X., ITO, K. & LUBKIN, S. R. 2006 An augmented approach for the pressure boundary condition in a Stokes flow. *Commun. Comput. Phys.* **1**, 874–885.

MENEGHINI, J. R., SALTARA, F., SIQIERA, C. L. R. & FERRARI, J. A. JR 2000 Numerical simulation of flow interference between two circular cylinders in tandem and side-by-side arrangements. *J. Fluids Struct.* **15**, 327–350.

METZGER, B., NICOLAS, M. & GUAZZELLI, É. 2007 Falling clouds of particles in viscous fluids. *J. Fluid Mech.* **580**, 283–301.

NIWA, H. S. 1994 Self-organizing dynamic model of fish schooling. *J. Theor. Biol.* **171** (2), 123–136.

PEDLEY, T. J. & KESSLER, J. O. 1992 Hydrodynamic phenomena in suspensions of swimming microorganisms. *Annu. Rev. Fluid Mech.* **24**, 313–358.

PESAVENTO, U. & WANG, Z. J. 2004 Falling paper: Navier–Stokes solutions, model of fluid forces, and centre of mass elevation. *Phys. Rev. Lett.* **93** (14), 144501.

SAINTILLAN, D. & SHELLEY, M. 2008 Instabilities and pattern formation in active particle suspensions: kinetic theory and continuum simulations. *Phys. Rev. Lett* **100**, 178103.

SINGH, P., CAUSSIGNAC, P. H., FORTES, A. F., JOSEPH, D. D. & LUNDGREN, T. S. 1989 Stability of periodic arrays of cylinders across the stream by direct numerical simulation. *J. Fluid Mech.* **205**, 553–571.

THIFFEAULT, J.-L. & CHILDRESS, S. 2010 Stirring by swimming bodies. *Phys. Lett.* A **374** (34), 3487–3490.

WANG, Z. J. & RUSSELL, D. 2007 Effect of forewing and hindwing interactions on aerodynamic forces and power in hovering dragonfly flight. *Phys. Rev. Lett.* **99**, 148101.

WARHAFT, Z. 2009 Laboratory studies of droplets in turbulence: towards understanding the formation of clouds. *Fluid Dyn. Res.* **41**, 011201.

XU, S. 2008 The immersed interface method for simulating prescribed motion of rigid objects in an incompressible viscous flow. *J. Comput. Phys.* **227**, 5045–5071.

XU, S. & WANG, Z. J. 2006*a* An immersed interface method for simulating the interaction of a fluid with moving boundaries. *J. Comput. Phys.* **216**, 454–493.

XU, S. & WANG, Z. J. 2006*b* Systematic derivation of jump conditions for the immersed interface method in three-dimensional flow simulation. *SIAM* **27** (6), 1948–1980.

XU, S. & WANG, Z. J. 2007 A 3D immersed interface method for fluid–solid interaction. *Comput. Meth. Appl. Mech. Engng* **197**, 2068–2086.